Structural and electric transport properties of gray arsenic under high pressure

Wenjing Cheng,[1,*] Xiaodong Yao,[1,*] Lingxiao Zhao,[1,*] Chenkai Li,[1] Qunfei Zheng,[1] Jun Han,[1] Shanmin Wang,[1,2] Ying Liu,[2,1,†] and Jinlong Zhu[1,2,‡]

[1]*Department of Physics, Southern University of Science and Technology, Shenzhen 518055, China*

[2]*Quantum Science Center of Guangdong-Hong Kong-Macao Greater Bay Area (Guangdong), Shenzhen 518045, People's Republic of China*

(Received 23 August 2023; revised 21 November 2023; accepted 31 January 2024; published 15 February 2024)

Gray arsenic is a two-dimensional semimetal material that has attracted much attention due to its rich and fascinating properties such as ultrahigh carrier mobility and giant magnetoresistance properties. In this work, the structural and electrical properties of gray arsenic under high pressure have been systematically explored. Two structural phase transitions, A7 phase of gray arsenic to simple cubic phase and simple cubic phase to host-guest phase, were revealed at ∼28 and ∼35 GPa, respectively. And the transition to host-guest phase completed at ∼46 GPa. Superconductivity appeared after ∼35 GPa and the maximum of T_c, ∼5 K, was revealed in pure host-guest phase at ∼54 GPa, which is currently the highest recorded T_c of arsenic. The anisotropic upper critical field of superconductivities revealed the presence of mixed phase and the relative crystal orientations of the high-pressure phases.

DOI: 10.1103/PhysRevB.109.064507

I. INTRODUCTION

Since the successful production of graphene by exfoliation in 2004, there has been a research boom in the field of two-dimensional (2D) materials [1–6]. As a fundamental member of the 2D material family, 2D crystals of VA-group single elements, such as phosphorus, arsenic, antimony, and bismuth, have been widely studied due to their excellent physical properties [7–11]. Black phosphorus is widely used in nano-optoelectronic technology due to its adjustable bandgap, high carrier mobility, and large on/off ratio [12–15]. In addition, arsenic has a phosphorus-like electronic system and may exhibit similar structures and properties, while its chemical properties are much more stable [16,17].

Gray arsenic (g-As), as the most abundant and stable allotropy of arsenic, is a layered A7 phase [10,18]. Recent theoretical calculations have shown that a few layers of gray arsenic have flexible bandgap, which can be adjusted by the number of layers or stress [19,20]. In contrast, bulk gray arsenic, as a semimetal, which exhibits rich and fascinating properties, such as its ultrahigh carrier mobility and giant magnetoresistance (GMR) properties from compensation mechanisms, attracts great attention [21,22].

Hydrostatic pressure has been widely used to tune the crystal and electronic structure [23–31]. Under pressure, all VA-group elements, P, As, Sb, and Bi, exhibit a similar phase transition process, passing through multiple phases from the rhombohedral phase (A7) at ambient pressure to the body-centered-cubic phase [32,33]. During this interval, different from P, the heavier elements (As, Sb, and Bi) undergo an incommensurate host-guest (HG) phase, such as As-III, Sb-IV, Sb-II, and Bi-III phases [34]. The unusual HG structure of an element under high pressure has attracted much attention since it was discovered [35–38]; especially the recent discovery of strong-coupling superconductivity in the Bi-III phase [36]. However, the research on the HG phase in As is limited, especially in terms of electrical transport properties. It is possibly due to the higher pressure required to access the HG phase in As [34]. In addition, as a semimetal, there is still a lack of research on the magnetic resistance, carrier mobility, and carrier density of gray arsenic under high pressure.

In this work, a systematic study was conducted on the structural and electromagnetic transport properties of gray arsenic single crystals under high pressure. Two structural phase transitions, the A7 phase of gray arsenic to simple cubic (SC) phase and the SC to HG phase, were revealed at ∼28 and ∼35 GPa, respectively. And the transition to HG phase completed at ∼46 GPa. Interestingly, two new characteristic Raman peaks in the HG phase were revealed. Specifically, the superconductivity was revealed after ∼35 GPa, attributed to the structural phase transition from SC to HG. The upper critical field related to angle under different pressures is considered as evidence of the SC+HG mixed phase. In addition, the magnetoresistance, carrier mobility, and carrier density at low temperatures under high pressure were obtained.

A. Raman

Raman spectroscopy studies structural information in crystals through the interaction between photons and lattice vibrations and is widely used for high-pressure research. The g-As has three Raman-active modes, namely, an A_{1g} mode that vibrates out of plane at $\sim 250\,\mathrm{cm}-1$ and an E_g mode that vibrates in plane at $\sim 190\,\mathrm{cm}^{-1}$ (double degeneracy). The Raman spectra of g-As under different pressures are shown

*These authors contributed equally to this work.
†Corresponding author: liuying@quantumsc.cn
‡Corresponding author: zhujl@sustech.edu.cn

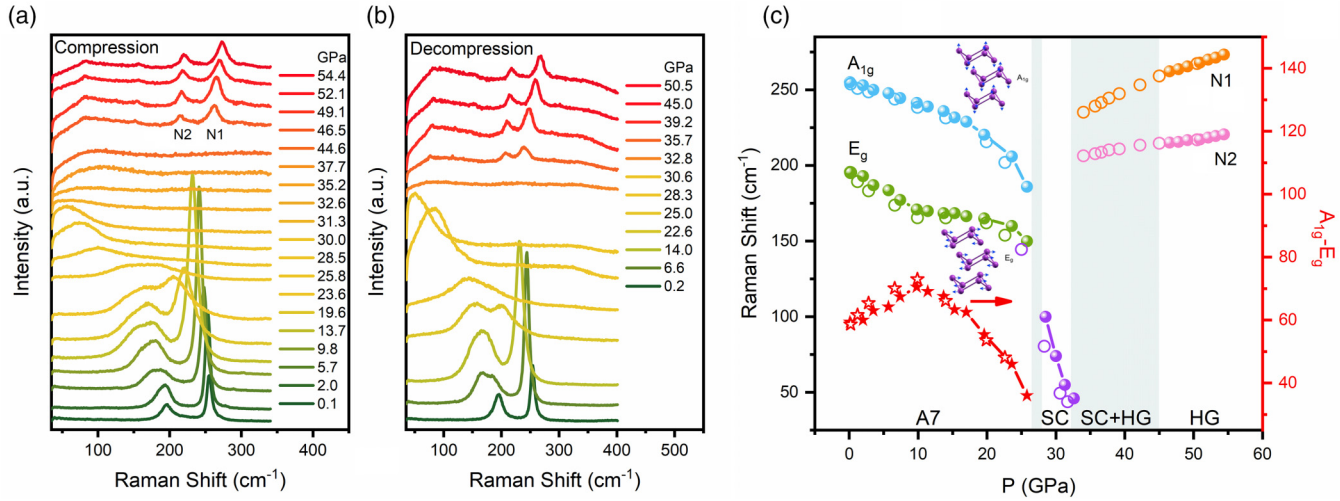

FIG. 1. Raman spectra of g-As single crystals in (a) compression and (b) decompression. (c) Raman shift as a function of pressure. Below 28 GPa, it exhibits two Raman modes of A7-As (blue dots represent the A_{1g} mode; green dots represent the E_g mode). The red stars represent the difference of Raman frequency $D_\omega = \omega(A_{1g}) - \omega(E_g)$. In SC-As ranging from 28 to 35 GPa, only one weak and wide new mode (purple dots) was observed, while in HG-As, there were two distinct Raman peaks, named N1 (orange dots) and N2 (pink dots), respectively. The shaded area is a guide for the eyes. Solid dots represent compression data, while hollow circles represent decompression data. The inset shows the schematic diagram of the Raman vibration mode.

in Fig. 1(a), with the pressure increasing to 54.4 GPa. At a pressure range of up to ∼28 GPa, the Raman spectrum of gray arsenic only undergoes a redshift, indicating that the A7 structure remains stable within this pressure range. At ∼28 GPa, the characteristic peak of A7-As is replaced by a weak and wide peak, indicating a transition from A7 to SC. In the SC mode, the peak further redshifts until it cannot be detected at ∼35 GPa. Until ∼46 GPa, two new clear and visible Raman peaks appeared. It suggested that another phase transition occurred and the new structure was considered to be the HG structure. The research on Raman spectroscopy of the HG phase in As is limited, and there are no vibration modes that have been assigned to these two peaks. The HG structure of As is described as a body-centered monoclinic host cell of the space group $I2/c$ and body-centered monoclinic guest cell of the space group $I2/m$ [34]. This structural phase transition has been theoretically and experimentally confirmed to occur at ∼41–50 GPa using x-ray diffraction (XRD) and has a range of mixing phase processes [32,34,37,39]. By combining behavior during compression and decompression, we believe that a structural phase transition from SC to HG occurred at ∼35 GPa, and the mixed phase of the two remained until ∼46 GPa, followed by only the HG phase. As the pressure increases until 54.4 GPa, the two Raman peaks of the HG phase show a blueshift, and no new phase appears.

The pressure dependence of the Raman mode frequency in the A7 phase and the SC phase is shown in Fig. 1(c). Before 10 GPa, compared to the A_{1g} mode with a decrease rate of 1.44 cm^{-1} /GPa, the frequency of the E_g mode decreases faster by 2.52 cm^{-1} /GPa. At 10 GPa, the redshift rates of A_{1g} and E_g modes changed. Compared with that below 10 GPa, the redshift rate of the A_{1g} mode increased to 2.71 cm^{-1} /GPa, while the rate of the E_g mode decreased to 0.59 cm^{-1} /GPa. The red stars show the difference of Raman frequency $D_\omega = \omega(A_{1g}) - \omega(E_g)$ of the A7 phase as a function of pressure. The frequency difference D_ω increases from 60 cm^{-1} under ambient pressure to ∼70 cm^{-1} at 10 GPa, then remains almost constant to 12.5 GPa, and then decreases to ∼40 cm^{-1} at 26 GPa as the increase of pressure. Although there is no obvious abnormal behavior in the Raman spectrum near 10 GPa, the changes in redshift rate revealed the changes in response by out-of-plane compression and in-plane compression to pressure, which may be due to slight structural distortions, such as the influence of subtle changes in the nearest neighbor and sub-nearest neighbor bond lengths on the Raman spectrum [40]. In addition, the Raman shift in decompression shows that all phase transitions and the structural distortion are reversible.

B. Electromagnetic transport

The Montgomery four-probe method was used for electromagnetic transport measurement [41,42]. Figure 2(a) shows the resistance as a function of temperature under different pressures. Before reaching 35 GPa, the increase in residual resistance ratio (RRR $= R_{300\,K}/R_{12\,K}$) [as shown in Fig. 2(c)] indicates that the metallic properties become increasingly apparent. It is noted that there are jumps in RRR both in the points of A7-SC and SC-HG phase transitions. Interestingly, after the SC-HG transition, ∼35 GPa, the zero-resistance state appears at low temperatures, indicating the possibility of superconductivity. To validate the superconductivity, a temperature dependence of resistance under different magnetic fields at 35.3 GPa was studied, as shown in Fig. 2(b). With the increase of magnetic fields, the superconducting properties are gradually suppressed until they disappear. The evolution of superconducting critical temperature (T_c) with pressure is shown in Fig. 2(d). The "90% standard" is adopted, where T_c is defined as the temperature with a resistance of 90% of the normal-state resistance, and the errors come from the fluctuation of data and noise of testing. Our results show a unique variation of T_c with pressure. As the pressure increases, T_c first

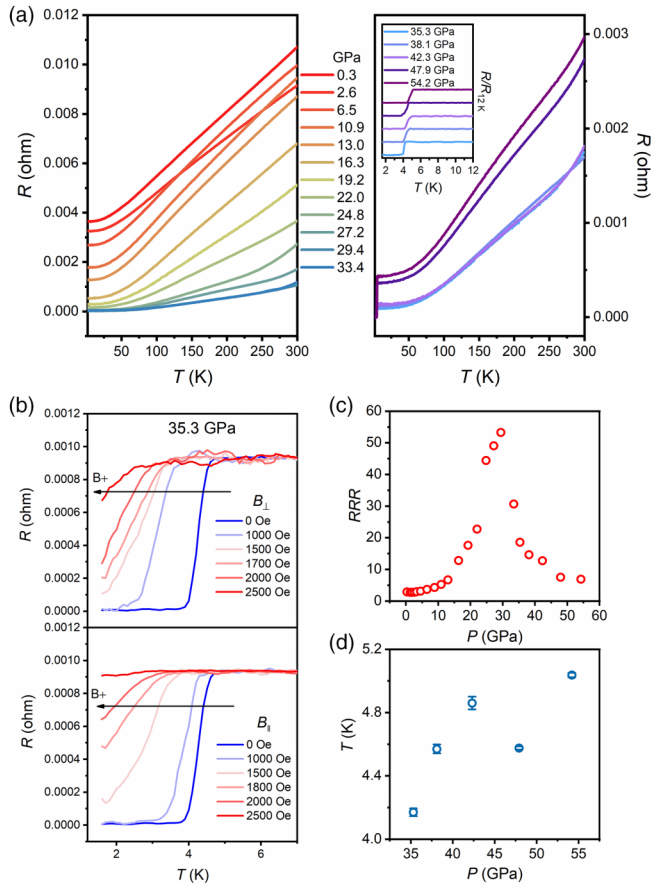

FIG. 2. (a) Temperature dependence of in-plane resistance at different pressures and normalized resistance $R/R_{12\,\mathrm{K}}$ vs T ranging from 1.6 to 12 K embedded under selected pressures. (b) Magnetic field dependence of superconducting transition temperatures measured at 35.3 GPa with field direction perpendicular ($B_\perp$) and parallel ($B_\parallel$) to the sample plane. (c) RRR (residual resistivity ratio) and (d) T_c as a function of pressure.

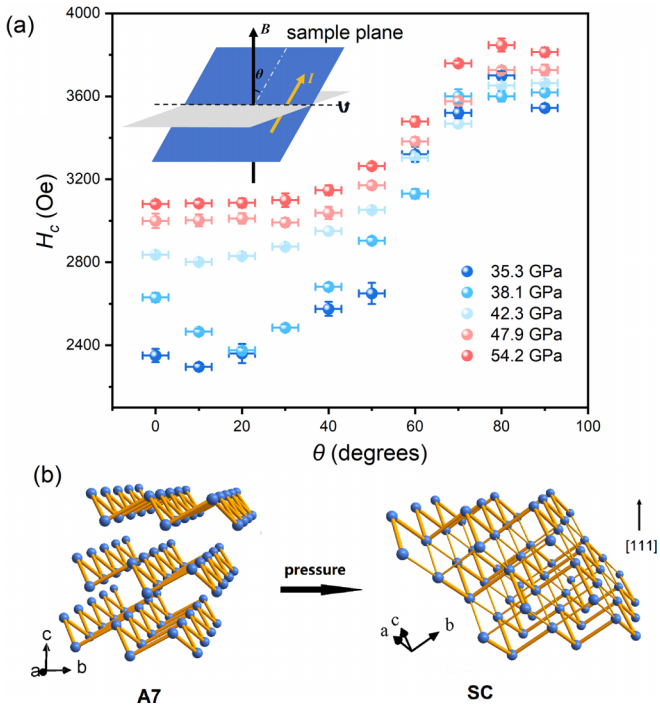

FIG. 3. (a) Angular dependence of the upper critical field under different pressures at 1.6 K (the error of θ is caused by the accuracy of the rotator, while the error of H_c is the same as discussed in T_c). The inset diagram shows the configuration of the sample and magnetic field and θ represents the angle between the magnetic field and the sample plane, meaning current. (b) Schematic diagram of structural phase transition of the A7-SC process.

rapidly increases, reaching 4.9 K at ∼43 GPa, then decreases to 4.6 K at ∼48 GPa, and then rises to 5 K at ∼54 GPa. The emergence of superconductivity is attributed to the beginning of the structural phase transition from SC to HG, and the drop of T_c at ∼48 GPa marks the completion of the structural phase transition. In addition, the maximum T_c, ∼5 K in the HG phase at ∼54 GPa, is higher than the prediction of temperature superconductivity of the body-centered tetragonal structure of As, with a T_c of 4.2 K at 150 GPa [37]. In addition, the upper critical field H_c was measured perpendicular to the sample plane varying the field under pressure as shown in Fig. S1 and discussed in the Supplemental Material [43].

In addition, a slight broadening of the superconducting transition under field was noticed as shown in Fig. 2(b). This broadening is common in superconductors, and the mechanisms are various [44]. In a 2D superconductor, like $YBa_2Cu_3O_{7-\delta}$ (YBCO), the major reason is vortex effect [45,46]. For MgB_2, superconducting fluctuation may have a significant impact [47]. In addition, there are influences from inhomogeneity of crystals or chemical components [48,49] and surface superconductivity [50]. As shown in Fig. S2 [43], the broadening was not increasing with pressure, which suggested that the reason for broadening is not due to inhomogeneity of the sample from the potential inhomogeneity of pressure. In order to clarify the origin of broadening in As, further experiments or theories are needed, such as calculation of the effect of thermal fluctuation or the measurement of magnetic susceptibility to reveal vortices.

In order to understand the generation of higher T_c, the density of state and electron-phonon coupling parameter are crucial. According to the calculation, the electronic structure of the HG phase is similar to that of the SC phase [32]. The Fermi velocities through fitting by T_c and coherence length are shown in Table S1 [43]. The low Fermi velocity suggests the high density of state at the Fermi level. In addition, similar to the HG phase in Bi [36], the low-energy phonons in the HG structure may result in strong electron-phonon coupling. The high density of state of strong electron-phonon coupling are beneficial for the improvement of T_c. In addition, further calculations of the electronic structure, phonon frequency, and electron-phonon coupling of the HG phase in As are necessary for understanding the superconductivity in the HG phase.

Meanwhile, in Fig. 2(b), we note the anisotropy of the upper critical field. Therefore, we investigated the correlation between the upper critical field (H_c) and the angle between the magnetic field and the sample plane (θ) at 1.6 K as shown in Fig. 3(a) (the inset figure is a schematic diagram of the sample and magnetic field configuration). The "95% standard" is adopted, where H_c is defined as a magnetic field with a resistance of 95% of the normal-state resistance. Before 48 GPa,

the upper critical field as a function of angle decreased first and then increased. This strange behavior is reminiscent of the anisotropy of a SC structure. The upper critical field takes the maximum value in the [111] direction (90°) and the minimum value in the [100] direction (∼35°) in the SC phase [23,51–53]. The *c* axis of the A7 phase transitions to the [111] direction of SC under pressure as shown in Fig. 3(b) [40]. Therefore, the anisotropy of the upper critical field is affected by the residual SC phase in the mixed phase before 48 GPa. After 48 GPa, the upper critical field approximately monotonically increases with angle, which suggests the transition to a pure HG phase from a mixed phase. And the approximately monotonic behavior indicates that the crystal orientation of the HG phase is parallel or perpendicular to the A7 phase.

One of the most attractive properties of g-As is the GMR effect. As shown in Fig. S3 [43], the MR up to 420 000% at 9 T was observed at 1.8 K under ambient pressure. Surprisingly and unfortunately, the GMR disappeared at very low pressure, 0.3 GPa, as shown in Fig. S4 [43]. Under pressure, the MR of g-As settled in ∼1.5% at 9 T. In addition, the Hall resistance within the selected pressure range is shown in Fig. S5 [43]. Unlike the two-band characteristic under ambient [21], the Hall resistance of the gray arsenic single crystal under pressure exhibits a linear field dependence under high pressure, indicating that g-As has a single-band characteristic of hole under high pressure, and hole carriers play a role in the main conductive transport properties. The carrier density and carrier mobility of hole were obtained through Hall resistance [54], as shown in Fig. S6 [43]. With the increase of pressure, the hole carrier density decreases and remains stable until ∼10 GPa, then rapidly increases, and the trend of hole carrier mobility is opposite. The turning point of hole carrier density at ∼10 GPa is caused by the slight structural distortion mentioned above.

II. CONCLUSION

In summary, a detailed study was conducted on the structure and electromagnetic transport properties of gray arsenic single crystal. At ∼10 GPa, a slight structural distortion happened, which is evidenced through turning points of redshift of Raman peaks and hole carrier density. With the increase of pressure, the hole carrier density decreases and remains stable until 10 GPa, then rapidly increases, while the trend of hole carrier mobility is opposite. The Raman characteristic peaks of g-As are presented above 46 GPa, located at 215 and 262 cm^{-1}, respectively. Two structural phase transitions of gray arsenic, A7-SC and SC-HG, were revealed at ∼28 and ∼35 GPa, respectively. And the SC-HG transition finished at ∼46 GPa. At the appearance of HG phase, the superconductivity was revealed, and the T_c achieved a maximum of ∼5 K at ∼54 GPa. The angle-dependent upper critical field revealed the presence of mixed phase and the relative crystal orientations of the high-pressure phases.

III. METHOD

The high-quality single crystals of gray As in this experiment were grown using a modified Bridgman technique. The As lumps (99.9999%) were purified and then loaded into a tapered quartz tube and was sealed under high vacuum. The sealed tube was placed vertically inside a muffle furnace, and was heated to 820°C at a rate of 40°C/h and held for a duration of 10 h before cooling slowly to 500°C at 1°C/h. Then the furnace is cooled down to room temperature at 10°C/h. Energy dispersive x-ray (EDX) spectrum and single-crystal XRD were used to determine the quality of single-crystal g-As, as shown in Fig. S7 and Table S2 [43] (see also Refs. [55,56] therein). The results of EDX indicate that the weight content of the As element in our sample is higher than 99%, and a small amount of oxygen in the surface originates from the environmental impact during sample preparation and characterization. The refined results and lattice constants can be found in Table S2 [43] (see also Refs. [55,56] therein).

Hydrostatic pressure is generated by a diamond-anvil cell (DAC) with a diameter of 300 μm. Stainless steel T301, prepressed to a thickness of 30 μm and drilled with a hole of 150 μm in diameter, was selected as the sealing gasket. A Raman spectrum is obtained by backscatter configuration through a 5-μm focus microscope and 1200 g/mm grating. Electromagnetic transport testing requires cubic boron nitride insulation on the gasket. NaCl as pressure transfer media have been applied both to Raman spectroscopy testing and electromagnetic transport testing. The van der Pauw four-electrode method is applied to the electromagnetic transport of gray arsenic in single crystal, and a triangular Pt sheet is selected as the electrode. The details are as follows: the sample is placed in the pressure transfer medium, and the four Pt electrodes are located between the sample and the diamond. The *ab* plane of the sample is placed parallel to the culet of the anvil. The angle between the magnetic field and the sample plane is adjusted by rotating the DAC through a horizontal rotator. In this experiment, the pressure was calibrated by the peak position of the ruby fluorescence peak [57].

ACKNOWLEDGMENTS

This work was supported in part by the National Natural Science Foundation of China under Grants No. 12274193 and No. 12004161, the National Key R&D Program of China under Grant No. 2018YFA0305703, and the Guangdong Basic and Applied Basic Research Foundation under Grant No. 2022A1515010044. J.Z. and Y.L. also acknowledge the Major Science and Technology Infrastructure Project of Material Genome Big-Science Facilities Platform supported by the Municipal Development and Reform Commission of Shenzhen. Some experiments are supported by the Synergic Extreme Condition User Facility.

[1] K. S. Novoselov, A. K. Geim, S. V. Morozov, D. Jiang, Y. Zhang, S. V. Dubonos, I. V. Grigorieva, and A. A. Firsov, Electric field effect in atomically thin carbon films, Science **306**, 666 (2004).

[2] S. Cahangirov, M. Topsakal, E. Aktürk, H. Şahin, and S. Ciraci, Two- and one-dimensional honeycomb structures of silicon and germanium, Phys. Rev. Lett. **102**, 236804 (2009).

[3] F. Ersan, D. Kecik, V. O. Özçelik, Y. Kadioglu, O. Ü. Aktürk, E. Durgun, E. Aktürk, and S. Ciraci, Two-dimensional pnictogens: A review of recent progresses and future research directions, Appl. Phys. Rev. **6**, 021308 (2019).

[4] J. R. Brent, N. Savjani, E. A. Lewis, S. J. Haigh, D. J. Lewis, and P. O'Brien, Production of few-layer phosphorene by liquid exfoliation of black phosphorus, Chem. Commun. (Cambridge, UK) **50**, 13338 (2014).

[5] L. Zhang, H. Huang, B. Zhang, M. Gu, D. Zhao, X. Zhao, L. Li, J. Zhou, K. Wu, Y. Cheng *et al.*, Structure and properties of violet phosphorus and its phosphorene exfoliation, Angew. Chem. Int. Ed. Engl. **59**, 1074 (2020).

[6] Y. Hu, Z.-H. Qi, J. Lu, R. Chen, M. Zou, T. Chen, W. Zhang, Y. Wang, X. Xue, J. Ma *et al.*, van der Waals epitaxial growth and interfacial passivation of two-dimensional single-crystalline few-layer gray arsenic nanoflakes, Chem. Mater. **31**, 4524 (2019).

[7] M. J. Duggin, A high-pressure phase in arsenic and its relation to pressure-induced phase changes in group 5B elements, J. Phys. Chem. Solids **33**, 1267 (1972).

[8] S. Zhang, M. Xie, F. Li, Z. Yan, Y. Li, E. Kan, W. Liu, Z. Chen, and H. Zeng, Semiconducting group 15 monolayers: A broad range of band gaps and high carrier mobilities, Angew. Chem. **128**, 1698 (2016).

[9] Z. Wu and J. Hao, Electrical transport properties in group-V elemental ultrathin 2D layers, npj 2D Mater. Appl. **4**, 4 (2020).

[10] J. Sturala, Z. Sofer, and M. Pumera, Chemistry of layered pnictogens: Phosphorus, arsenic, antimony, and bismuth, Angew. Chem. Int. Ed. **58**, 7551 (2019).

[11] F. Ersan, E. Aktürk, and S. Ciraci, Stable single-layer structure of group-V elements, Phys. Rev. B **94**, 245417 (2016).

[12] X. Ling, H. Wang, S. Huang, F. Xia, and M. S. Dresselhaus, The renaissance of black phosphorus, Proc. Natl. Acad. Sci. USA **112**, 4523 (2015).

[13] L. Li, Y. Yu, G. J. Ye, Q. Ge, X. Ou, H. Wu, D. Feng, X. H. Chen, and Y. Zhang, Black phosphorus field-effect transistors, Nat. Nanotechnol. **9**, 372 (2014).

[14] S. Zhang, S. Guo, Z. Chen, Y. Wang, H. Gao, J. Gómez-Herrero, P. Ares, F. Zamora, Z. Zhu, and H. Zeng, Recent progress in 2D group-VA semiconductors: From theory to experiment, Chem. Soc. Rev. **47**, 982 (2018).

[15] F. Xia, H. Wang, and Y. Jia, Rediscovering black phosphorus as an anisotropic layered material for optoelectronics and electronics, Nat. Commun. **5**, 4458 (2014).

[16] M. Zhong, Q. Xia, L. Pan, Y. Liu, Y. Chen, H.-X. Deng, J. Li, and Z. Wei, Thickness-dependent carrier transport characteristics of a new 2D elemental semiconductor: Black arsenic, Adv. Funct. Mater. **28**, 1802581 (2018).

[17] Y. Chen, C. Chen, R. Kealhofer, H. Liu, Z. Yuan, L. Jiang, J. Suh, J. Park, C. Ko, H. S. Choe *et al.*, Black arsenic: A layered semiconductor with extreme in-plane anisotropy, Adv. Mater. **30**, 1800754 (2018).

[18] N. Antonatos, V. Mazánek, P. Lazar, J. Sturala, and Z. Sofer, Acetonitrile-assisted exfoliation of layered grey and black arsenic: Contrasting properties, Nanoscale Adv. **2**, 1282 (2020).

[19] Z. Zhu, J. Guan, and D. Tománek, Strain-induced metal-semiconductor transition in monolayers and bilayers of gray arsenic: A computational study, Phys. Rev. B **91**, 161404(R) (2015).

[20] S. Zhang, Z. Yan, Y. Li, Z. Chen, and H. Zeng, Atomically thin arsenene and antimonene: Semimetal–semiconductor and indirect–direct band-gap transitions, Angew. Chem. Int. Ed. **54**, 3112 (2015).

[21] L. Zhao, Q. Xu, X. Wang, J. He, J. Li, H. Yang, Y. Long, D. Chen, H. Liang, C. Li *et al.*, Magnetotransport properties in a compensated semimetal gray arsenic, Phys. Rev. B **95**, 115119 (2017).

[22] C. S. Ih and D. N. Langenberg, Azbel'-Kaner cyclotron resonance in arsenic, Phys. Rev. B **1**, 1425 (1970).

[23] W. Cheng, C. Li, Q. Zheng, J. Han, S. Wang, Y. Liu, and J. Zhu, Pressure-tuned structure and electric transport properties in violet phosphorus, Phys. Rev. B **107**, 184513 (2023).

[24] Z. Zhang, Z. Chen, Y. Zhou, Y. Yuan, S. Wang, J. Wang, H. Yang, C. An, L. Zhang, X. Zhu *et al.*, Pressure-induced reemergence of superconductivity in the topological kagome metal CsV_3Sb_5, Phys. Rev. B **103**, 224513 (2021).

[25] Z. Chi, X. Chen, F. Yen, F. Peng, Y. Zhou, J. Zhu, Y. Zhang, X. Liu, C. Lin, S. Chu *et al.*, Superconductivity in pristine $2H_a-MoS_2$ at ultrahigh pressure, Phys. Rev. Lett. **120**, 037002 (2018).

[26] B. Han, F. Li, L. Li, X. Huang, Y. Gong, X. Fu, H. Gao, Q. Zhou, and T. Cui, Correlatively dependent lattice and electronic structural evolutions in compressed monolayer tungsten disulfide, J. Phys. Chem. Lett. **8**, 941 (2017).

[27] Z. J. Xiang, G. J. Ye, C. Shang, B. Lei, N. Z. Wang, K. S. Yang, D. Y. Liu, F. B. Meng, X. G. Luo, L. J. Zou *et al.*, Pressure-induced electronic transition in black phosphorus, Phys. Rev. Lett. **115**, 186403 (2015).

[28] C. Li, Y. Liu, Q. Yang, Q. Zheng, Z. Yan, J. Han, J. Lin, S. Wang, J. Qi, Y. Liu *et al.*, Tuning of optical behavior in monolayer and bilayer molybdenum disulfide using hydrostatic pressure, J. Phys. Chem. Lett. **13**, 161 (2022).

[29] X. Ren, X. Yan, A. S. Ahmad, H. Cheng, Y. Li, Y. Zhao, L. Wang, and S. Wang, Pressure-induced phase transition and band gap engineering in propylammonium lead bromide perovskite, J. Phys. Chem. C **123**, 15204 (2019).

[30] F. Li, Y. Yan, B. Han, L. Li, X. Huang, M. Yao, Y. Gong, X. Jin, B. Liu, C. Zhu *et al.*, Pressure confinement effect in MoS_2 monolayers, Nanoscale **7**, 9075 (2015).

[31] Z.-H. Chi, X.-M. Zhao, H. Zhang, A. F. Goncharov, S. S. Lobanov, T. Kagayama, M. Sakata, and X.-J. Chen, Pressure-induced metallization of molybdenum disulfide, Phys. Rev. Lett. **113**, 036802 (2014).

[32] U. Häussermann, K. Söderberg, and R. Norrestam, Comparative study of the high-pressure behavior of As, Sb, and Bi, J. Am. Chem. Soc. **124**, 15359 (2002).

[33] J. A. Flores-Livas, A. Sanna, A. P. Drozdov, L. Boeri, G. Profeta, M. Eremets, and S. Goedecker, Interplay between structure and superconductivity: Metastable phases of phosphorus under pressure, Phys. Rev. Mater. **1**, 024802 (2017).

[34] O. Degtyareva, M. I. McMahon, and R. J. Nelmes, High-pressure structural studies of group-15 elements, High Pressure Res. **24**, 319 (2004).

[35] U. Häussermann, High-pressure structural trends of group 15 elements: Simple packed structures versus complex host–guest arrangements, Chem. -Eur. J. **9**, 1471 (2003).

[36] P. Brown, K. Semeniuk, D. Wang, B. Monserrat, C. J. Pickard, and F. M. Grosche, Strong coupling superconductivity in

a quasiperiodic host-guest structure, Sci. Adv. **4**, eaao4793 (2018).

[37] P. Tsuppayakorn-aek, W. Luo, R. Ahuja, and T. Bovornratanaraks, The high-pressure superconducting phase of arsenic, Sci. Rep. **8**, 3026 (2018).

[38] V. Heine, As weird as they come, Nature (London) **403**, 836 (2000).

[39] R. G. Greene, H. Luo, and A. L. Ruoff, bcc arsenic at 111 GPa: An x-ray structural study, Phys. Rev. B **51**, 597 (1995).

[40] H. J. Beister, K. Strossner, and K. Syassen, Rhombohedral to simple-cubic phase transition in arsenic under pressure, Phys. Rev. B **41**, 5535 (1990).

[41] H. C. Montgomery, Method for measuring electrical resistivity of anisotropic materials, J. Appl. Phys. **42**, 2971 (1971).

[42] L. J. v. d. Pauw, A method of measuring specific resistivity and Hall effect of discs of arbitrary shape, *Semiconductor Devices: Pioneering Papers* (World scientific, 1991), p. 174.

[43] See Supplemental Material at http://link.aps.org/supplemental/10.1103/PhysRevB.109.064507 for discussion of evolution of critical field, coherence length, and Ferimi energy with pressure; broadening of resistance transition under pressure; MR of g-As under ambient and high pressure; Hall resistance of g-As at 1.6 K under high pressure and evolution of carrier density and carrier mobility of hole under high pressure at 1.6 K; results of EDX and XRD; and the cif file of our sample

[44] J. E. Hirsch and F. Marsiglio, Unusual width of the superconducting transition in a hydride, Nature (London) **596**, E9 (2021).

[45] R. Liang, D. A. Bonn, and W. N. Hardy, Discontinuity of reversible magnetization in untwinned YBCO single crystals at the first order vortex melting transition, Phys. Rev. Lett. **76**, 835 (1996).

[46] D. G. Xenikos, J.-T. Kim, and T. R. Lemberger, Vortex correlations in the superconducting transition of $YBa_2(Cu_{1-x}Al_x)_3O_{7-\delta}$ films in high magnetic fields, Phys. Rev. B **48**, 7742 (1993).

[47] T. Masui, S. Lee, and S. Tajima, Origin of superconductivity transition broadening in MgB_2, Physica C (Amsterdam, Neth.) **383**, 299 (2003).

[48] A. K. Pradhan, Z. X. Shi, M. Tokunaga, T. Tamegai, Y. Takano, K. Togano, H. Kito, and H. Ihara, Electrical transport and anisotropic superconducting properties in single crystalline and dense polycrystalline MgB_2, Phys. Rev. B **64**, 212509 (2001).

[49] V. N. Zverev and V. F. Gantmakher, Broadening of superconducting resistive transition in macroscopically inhomogeneous Ga-Sb and Zn-Sb alloys under magnetic field, J. Exp. Theor. Phys. **83**, 122 (1996).

[50] A. Zeinali, T. Golod, and V. M. Krasnov, Surface superconductivity as the primary cause of broadening of superconducting transition in Nb films at high magnetic fields, Phys. Rev. B **94**, 214506 (2016).

[51] D. E. Farrell, B. S. Chandrasekhar, and S. Huang, Precision measurement of anisotropy in the upper critical field of superconducting niobium, Phys. Rev. **176**, 562 (1968).

[52] P. C. Hohenberg and N. R. Werthamer, Anisotropy and temperature dependence of the upper critical field of type-II superconductors, Phys. Rev. **153**, 493 (1967).

[53] H. W. Weber, E. Seidl, C. Laa, E. Schachinger, M. Prohammer, A. Junod, and D. Eckert, Anisotropy effects in superconducting niobium, Phys. Rev. B **44**, 7585 (1991).

[54] E. F. Schubert, *Doping in III-V Semiconductors*, Cambridge Studies in Semiconductor Physics and Microelectronic Engineering (Cambridge University Press, Cambridge, 1993).

[55] G. M. Sheldrick, *SHELXL-2014, Program for the Solution of Crystal Structures* (University of Göttingen, Göttingen, Germany, 2014).

[56] G. M. Sheldrick, SADABS, v.2.01, Bruker/Siemens Area Detector Absorption Correction Program, *Bruker AXS: Madison, Wisconsin*, 1998.

[57] G. Shen, Y. Wang, A. Dewaele, C. Wu, D. E. Fratanduono, J. Eggert, S. Klotz, K. F. Dziubek, P. Loubeyre, O. V. Fat'yanov *et al.*, Toward an international practical pressure scale: A proposal for an IPPS ruby gauge (IPPS-Ruby2020), High Pressure Res. **40**, 299 (2020).